Progress In Electromagnetics Research Letters, Vol. 130, 36–43, 2026

PIER Letters

*(Received 16 January 2026, Accepted 19 March 2026, Scheduled 29 April 2026)*

# Modulation Technique of Conformal Metasurface for 3D Spiral Shaped Near-Field with High SNR and Efficiency

Hui-Fen Huang[1,*] and Ke-Chun Niu[2]

[1] *School of Electronic and Information Engineering, South China University of Technology, Guangzhou 510641, China*
[2] *Hefei Branch, China Telecom Corporation Limited, Hefei 230088, China*

**ABSTRACT:** The curvature effects of curved metasurface (MTS) lead to oblique incidence and different unit radiation normal vectors (DURNVs). Oblique incidence causes a reduction in scattering amplitude and degrades focusing efficiency (FE), and DURNV distorts the radiation pattern of curved MTSs. To the knowledge of the authors, for the first time, this paper proposes a phase amplitude modulation and phase modulation (PAM-PM) combined modulation technique for cylindrical MTS to generate a high signal-to-noise ratio (SNR) and high FE three-dimensional (3D) shaped near field with a spiral cross-sectional shape. In addition, a near field with controllable spatial positions is a practical application requirement, and this paper provides a method to establish a 3D-shaped near field with controlled spatial positions. The proposed cylindrical MTS with PAM-PM modulation technique outperforms the PM technique significantly, achieving an SNR above 13 dB and an FE of 38.1%. For cylindrical MTS with only PM, there exists some noise, and the FE is 33.2%. This proposed modulation technique can be applied to 3D near-field systems based on conformal MTS, including wireless power transfer, radiometric temperature sensors for hyperthermia, and medical imaging systems.

## 1. INTRODUCTION

Point focus (FE) electric field and 2D focusing fields with controlled sizes and shapes are developed in the Fresnel region for wireless power transfer, radiometric temperature sensor for hyperthermia, and medical imaging systems, biomedicine, nondestructive testing, industrial heating, and biomedical imaging [1–7]. However, practical applications need 3D-shaped near field with the required size, shape, and spatial position because a 3D high-intensity focused field covering the target area can shorten the scanning time and obtain a high-resolution image for medical imaging, precise energy concentration in the target area without damaging the healthy tissues, effective near-field communication, multi-user wireless energy transfer, and highly efficient industrial heating. Currently, there are few reports on 3D-shaped near-field construction. An algorithm for designing a 3D pulsed caustic (accelerating) beam with helical trajectory is developed [8]. MTSs enable the manipulation of amplitude, phase, and polarization of electromagnetic fields. Various MTS devices have been studied with novel functionalities, such as holography [9] and negative refractive index [10]. MTS is also used in generating a 3D-shaped near field. A 3D caustic beam with helical trajectory is constructed by Huygens' MTS [11]. An arbitrary cross-section-shaped 3D near field is obtained in [12]. However, the above 3D field is produced by planar MTSs with PM. In addition, the start position of the 3D shaped near field is in $z = 0$ plane and is not located in an arbitrary $z$ coordinate spatial position. Conformal MTSs are widely used in missiles, unmanned aerial vehicles, and high-speed vehicles, and are candidates for communication systems and multifunction radars due to wide-angle beam-scanning capabilities [13, 14].

This paper has the following advantages: (1) Proposing a PAM-PM combined modulation strategy for the conformal MTS, which generates a 3D field with high SNR and FE. (2) Providing a method for generating the 3D shaped near field with an arbitrary cross-section shape and a controllable $z$ coordinate spatial position from $z_1$ to $z_2$. The paper is organized as follows. Section 2 is the design principle, and Section 3 provides the conformal MTS design. Simulated and measured results are in Section 4, and Section 5 is the conclusion.

## 2. DESIGN PRINCIPLE

### 2.1. Bessel Beam Theory

Figure 1 illustrates the conceptual framework for generating Bessel beams by an MTS. The physical parameters $D$, $\alpha$, and $Z_{\max}$ are the MTS aperture size, convergence angle, and 3-dB non-diffracting distance of the Bessel beam, respectively.

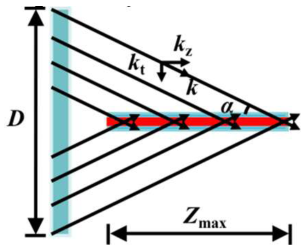

**FIGURE 1.** Schematic illustration of generating Bessel beams using a MTS.

---

[*] Corresponding author: Hui-Fen Huang (huanghf@scut.edu.cn).

In this paper, the parameters $\alpha$ and $Z_{\max}$ are set to 50° and 170 mm, respectively.

In cylindrical coordinates, the radial differential equation of the electric field is as follows [15].

$$E(\rho, z, t) = \exp\left(i\left(k_z z - wt\right)\right) J_0\left(k_r \rho\right) \tag{1}$$

where $J_0$ is the zeroth-order Bessel function; $k_z$ and $k_r$ are the longitudinal and transverse wave vectors, respectively, while $k$ and $\lambda$ denote the wave number and operating wavelength, respectively. The relationship between $k_z$ and $k_r$ is as follows [16].

$$k_r = \frac{2\pi}{\lambda}\sin\alpha = \sqrt{k^2 - k_z^2} \tag{2}$$

The relationship among $\alpha$, $D$, and $Z_{\max}$ is as follows:

$$Z_{\max} = \frac{D}{2\tan\alpha} \tag{3}$$

Theoretically, $Z_{\max} < 2D^2/\lambda$, and "$2D^2/\lambda$" is the radius of the near-field region. Then, the convergence angle $\alpha$ should satisfy the following condition:

$$\frac{\lambda}{4D} < \sin\alpha \leq 1 \tag{4}$$

## 2.2. 3D Shaped Near-Field Construction by Bessel Beam Array

Four steps for constructing a 3D-shaped field with an arbitrary cross section and $z$ coordinate spatial position (from $z_1$ to $z_2$) are as follows. First, the two-dimensional (2D) cross-section geometry shape (in the $xoy$ plane at $z = z_1$) of the designed 3D shaped near-field is drawn using a drawing software. Second, the coordinates of the discrete points ($x'_i, y'_i, z_1$) in the 2D cross-sectional geometry shape are extracted by the Matlab function "find". The coordinates of these discrete points are represented by a single-column matrix equation.

$$\begin{cases} X = \left\{x'_1, x'_2, x'_3, x'_4 \ldots x'_N\right\}^T & \text{for } x \text{ coordinates} \\ Y = \left\{y'_1, y'_2, y'_3, y'_4 \ldots y'_N\right\}^T & \text{for } y \text{ coordinates} \end{cases} \tag{5}$$

where $N$ is the discrete point number. Third, a diffraction-free Bessel beam array is generated by considering each discrete point ($x'_i$, $y'_i$, $z_1$) as the center of each Bessel beam element. Each Bessel beam element is obtained by setting the Bessel beam element radius $\rho = \sqrt{(x - x'_i)^2 + (y - y'_j)^2}$ in (1), where $(x, y)$ is the coordinates in the $xoy$ plane at $z = z_1$. Fourth, to generate a beautifully shaped field pattern, the radius $\rho$ is optimized under the condition $\rho_{optimized}$ <10, which is obtained according to the maximum SNR. According to the above four steps, an arbitrary cross-section-shaped 3D near field can be constructed using a Matlab program.

## 2.3. PAM-PM Technique

There are three types of wavefront manipulation techniques for MTS: PM, amplitude modulation, and PAM. (1) Compared with single PM or amplitude modulation (AM), PAM can significantly improve modulation resolution and SNR [17, 18]. (2) High amplitude efficiency is a key pursuit in relevant research; yet its realization is mainly limited by the traditional normal incidence assumption for all unit cells [19]. (3) The curvature effects of curved MTS mainly include two aspects: (*i*) Oblique incidence (especially $\theta > 40°$) causes scattering amplitude reduction and nonlinear phase effects, leading to degraded focusing efficiency (FE) and incomplete 360° phase coverage [19]; slight bending ($\theta < 40°$) shows almost the same phase range and loss as flat surfaces [20]. (*ii*) Local radiation angles skew toward the local normal vector, generating distorted radiation patterns and noise, while traditional PM further introduces noise due to the lack of amplitude regulation [21].

According to the above reference research findings, a PAM-PM combined modulation strategy is proposed to improve SNR and FE as follows: (1) PM with uniform amplitude is used for incidence angle $\theta < 40°$ for high efficiency. (2) PAM is used for $\theta > 40°$ by considering the oblique incidence effect induced by the MTS curvature effects for improving modulation resolution and SNR.

## 2.4. MTS Phase and Amplitude Distributions by Phase Conjugation (PC) Technique

The 3D-shaped configuration formed by a Bessel beam array through a Matlab program is imported into electromagnetic (EM) simulation software (such as Computer Simulation Technology (CST)). Then, the phase and amplitude distributions in the designed MTS are obtained through the PC technique. There are seven steps to design the MTS based on PC technique. **Step 1**. The established 3D-shaped Bessel beam array by the Matlab program is imported into the CST software, which acts as a test 3D-shaped $E$-field in CST. **Step 2**. Set up a recording plane with the same shape, dimensions, and position as the designed MTS in CST. **Step 3**. Divide the recording plane into meshes, which have the same size as the unit cells. **Step 4**. Record the test $E$-fields at the mesh positions. **Step 5**. The recorded test $E$-field at each mesh is operated PC. **Step 6**. The phase and amplitude distribution maps are obtained according to the phase conjugate electric fields. **Step 7**. The cylindrical conformal MTS is designed according to the phase and amplitude distributions and the proposed PAM-PA modulation strategy. The designed MTS is excited by a horn and generates a 3D-shaped $E$-field, which has the same shape and position as the test field.

# 3. MTS DESIGN

## 3.1. Unit Cell Design

The proposed unit cell in Fig. 2 is used to form the MTS, which consists of four metal layers separated by an FR4 substrate with permittivity 4.3 and thickness 0.04 mm. The 3D schematic view, two middle metal layers, and top (or bottom)

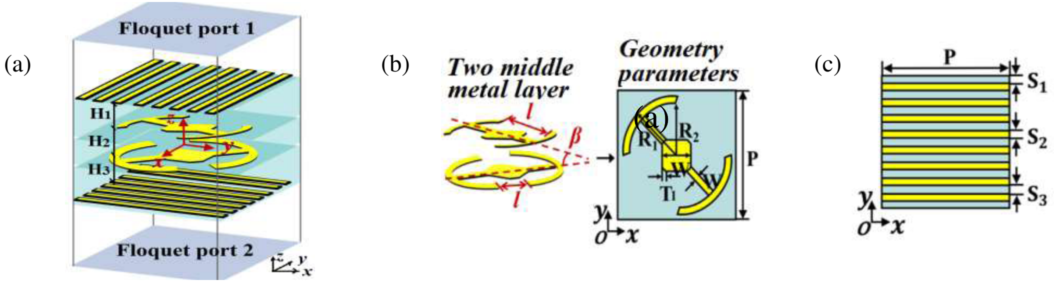

**FIGURE 2**. The proposed unit structure. (a) 3D schematic view. (b) Middle metal layer. (c) Top (or bottom) metal layer.

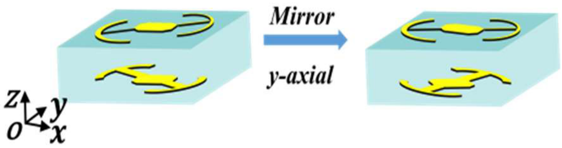

**FIGURE 3**. The proposed unit and its corresponding mirrored counterpart.

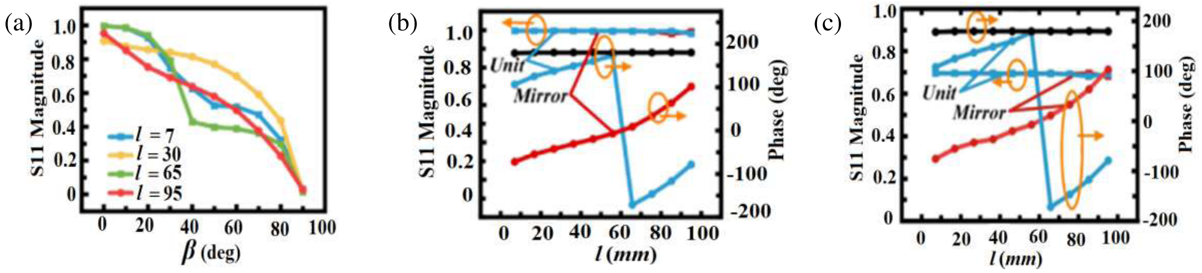

**FIGURE 4**. The curves of the proposed unit and its mirror part under $y$-polarized normal incidence at 12 GHz: (a) Transmission amplitude vs $\beta$ for different $l$ values for the unit and its mirror part; Transmission amplitude (or phase) vs $l$: for $\beta = 0^\circ$ (b), for $\beta = 45^\circ$ (c).

metal layer are shown in Figs. 2(a)–2(c), respectively. The top and bottom metal layers are two mutually orthogonal narrow rectangular stripes with the same size and are responsible for $y$- and $x$-polarization selections, respectively. The “◆”-like shaped two middle metal layers act as polarization conversion and PAM. The “◆”-like shaped metal patch is a composite structure of “⌶” and ⯃, which is a square patch with four isosceles triangles cut from the four vertices. The geometry parameters marked in Fig. 3 are as follows: $P = 5.85$ mm, $R_1 = 2.868$ mm, $R_2 = 2.363$ mm, $H_1 = 2.565$ mm, $H_2 = 1.665$ mm, $W = 0.315$ mm, $W_1 = 1.35$ mm, $S_1 = 0.36$ mm, $S_2 = 0.18$ mm, $S_3 = 0.495$ mm, $T = 0.18$ mm. The parameters $l$ and $\beta$ marked in Fig. 2(b) control the phase and amplitude, respectively. The 360° phase covering is achieved by both the unit and its mirror part (as in Fig. 3). The scattering parameter $S_{11}$ amplitude of the proposed unit cell is simulated by the software CST Studio Suite 2023 Floquet ports in the frequency domain as illustrated in Fig. 2(a) under $x$-polarized normal incidence from the bottom. The two middle metal layers convert the $x$-polarization to $y$-polarization. The amplitude and phase of $S_{11}$ can be obtained from the CST simulation curve of $S_{11}$ vs control geometry parameter ($\beta$ or $l$).

For amplitude modulation, Fig. 4(a) is the curve of scattering amplitude vs $\beta$ at 12 GHz for the proposed unit and its mirror part. The curves for the proposed unit and its mirror part overlap, which indicates that the scattering amplitude is adjusted by $\beta$ for both the unit and its mirror part. When $\beta$ varies from 90° to 0°, the transmission amplitude varies from 0 to 1. The curves in Fig. 4(a) overlap for different $l = 7$ mm, 30 mm, 65 mm, 95 mm, which indicates that different $l$ values do not affect the curve of scattering amplitude vs $\beta$. For phase modulation, Figs. 4(b) and 4(c) are the curves of scattering amplitude (or phase) vs geometry parameter $l$ for $\beta = 0$ and 45°, respectively. The following information is obtained: (1) The curve in blue is for the proposed unit. When $l$ increases from 0.315 mm to 4.275 mm, the phase for the proposed unit linearly increases from $-72^\circ$ to $101^\circ$ and a 180° phase range is covered. The curve in red is for the mirror part. When $l$ increases from 0.5 mm to 4.3 mm, the phase increases linearly from $-178^\circ$ to $-78^\circ$ and from 106° to 176°, and a 180° phase range is covered. The phase curves for the proposed unit and its mirror part are parallel to each other, have a 180° phase difference (black line), and a linear phase shift covering 360° is achieved by the unit and its mirror part. (2) The transmission amplitudes for the proposed unit and its mirror part are close to 1. The curves in Fig. 4 overlap for different $l$ values $l = 7$ mm, 30 mm, 65 mm, 95 mm or $\beta = 0^\circ$, 45°, which indicates that the amplitude and phase can be independently controlled by $\beta$ and $l$, respectively.

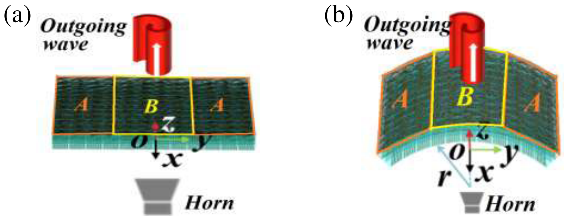

**FIGURE 5**. Schematic diagram of spiral-shaped 3D near-fields by: the planar MTS (a), and cylindrical conformal MTS (b).

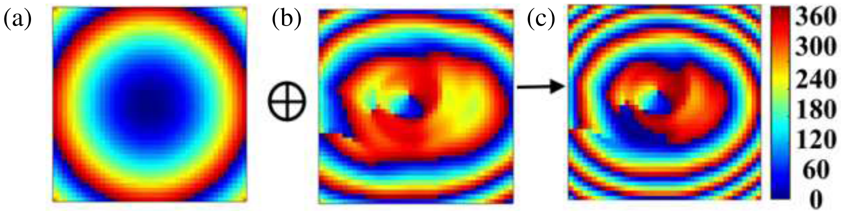

**FIGURE 6**. Compensated phase distributions for the planar MTS and the cylindrical conformal MTS located in $z = 0$ at 12 GHz: (a) for $\Phi_1$, (b) for $\Phi_2$ by PC, (c) for $\Phi$.

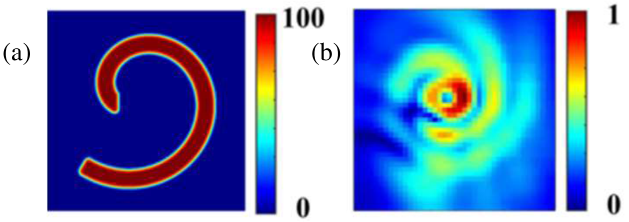

**FIGURE 7**. The cross section of the 3D shaped $E$-field at 12 GHz: in $xoy$ plane at $z = 110$ mm generated by Matlab (a), Normalized E-density distribution in the cylindrical conformal MTS by PC technique (b).

### 3.2. MTS Design

To confirm the PAM-PM combined design strategy for the conformal MTS with high SNR and FE, four transmission MTSs with the same size of 351 mm×351 mm ($14.04\lambda \times 14.04\lambda$, $\lambda$ wavelength) formed by $60 \times 60$ unit cells are researched and compared at 12 GHz: cylindrical conformal MTS-1 with PAM-PM technique (PAM in area A, PM in area B, marked in Fig. 5), planar MTS-2 (PAM in area-A, PM in area-B), cylindrical conformal MTS-3 with PM, and the planar MTS-4 with PM. The curvature radius of the cylindrical conformal MTS is $r = 350$ mm. Fig. 5 illustrates a schematic diagram of the spiral-shaped 3D propagation near fields with spiral-shaped cross section (in $xoy$ plane) and linear propagation trajectory (in $z$ coordinate axis direction) generated by the planar or cylindrical conformal phase-gradient MTSs. The axis of the cylindrical conformal MTS with radius $r$ is along the $x$-axis. The MTSs are excited by a horn whose 3 dB beamwidth is 27.2°. The optimization ratio of focal distance/aperture diameter is 1.31. The compensated phase is $\Phi = \Phi_1 + \Phi_2$, where $\Phi_1$ is the compensated phase for transferring the spherical wave from the horn into the plane wave, and $\Phi_2$ converts the plane wave into the 3D-shaped near field. PC technique is used to obtain $\Phi_2$ and the amplitude. All simulated results are obtained by CST.

(1) For the cylindrical conformal MTS. Figs. 6(a)–6(c) are the compensated phase distributions for $\Phi_1$, $\Phi_2$, and the total compensated phase $\Phi$ in the cylindrical conformal MTS, respectively. $\Phi_2$ is obtained by PC technique. The $E$-field distributions of the cross sections in the $xoy$ plane are shown in Fig. 7. Fig. 7(a) is the $E$-field distribution at $z = 110$ mm generated by Matlab, and Fig. 7(b) is the normalized $E$-density distribution in the cylindrical conformal MTS obtained by PC technique.

(2) For the planar MTS. Figs. 8(a)–8(c) are the compensated phase distributions for $\Phi_1$, $\Phi_2$, and the total compensated phase $\Phi$ in the planar MTS located in $z = 0$, respectively. The $E$-field distributions of the cross sections in the $xoy$ plane are shown in Fig. 9. Fig. 9(a) is the $E$-field distribution in the $xoy$ plane at $z = 110$ mm generated by Matlab, and Fig. 9(b) is the normalized $E$-density distribution in the planar MTS obtained by the PC technique.

The distribution maps for the control geometry parameters are in Fig. 10 and Fig. 11. For the cylindrical conformal MTS-1 (PAM in area-A and PM in area-B): According to Fig. 4, Fig. 6(c), and Fig. 7(b), the distribution maps for the control geometry parameters ($\beta$, $l$) are shown in Figs. 10(a) and 10(b), respectively. Fig. 10(c) is the unit and mirror unit distribution map, and “0” and “1” represent the unit and mirror unit, respectively. For the planar MTS-2 (PAM in area-A and PM in area-B): According to Fig. 4, Fig. 8(c), and Fig. 9(b), the distribution maps for the control geometry parameter ($\beta$, $l$) are shown in Figs. 11(a), 11(b), respectively. Fig. 11(c) is the unit and mirror unit distribution map.

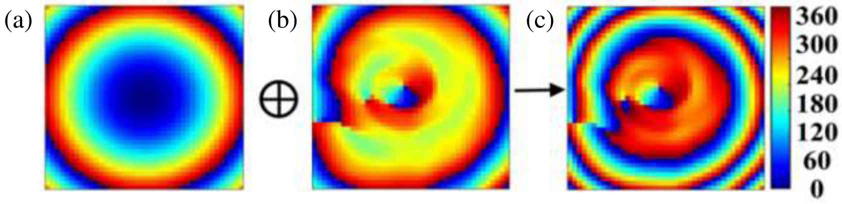

**FIGURE 8.** Compensated phase distributions for the planar MTS at 12 GHz: (a) for $\Phi_1$, (b) for $\Phi_2$ by PC, (c) for $\Phi$.

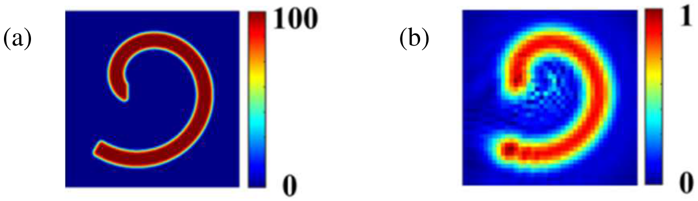

**FIGURE 9.** The cross-section-shaped $E$-field distributions for the planar MTS at 12 GHz: (a) in $z = 110$ mm generated by Matlab, (b) Normalized $E$-density distribution in the MTS by PC technique.

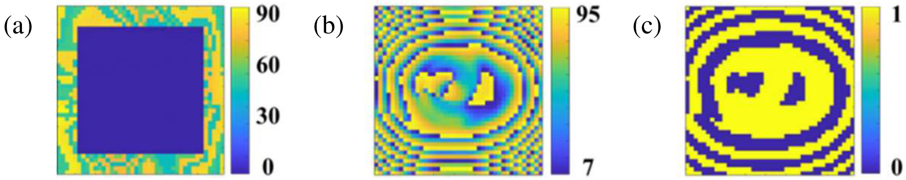

**FIGURE 10.** The geometry parameter distributions for the cylindrical conformal MTS: (a) for $\beta$, (b) for $l$, and (c) for the unit and mirror unit.

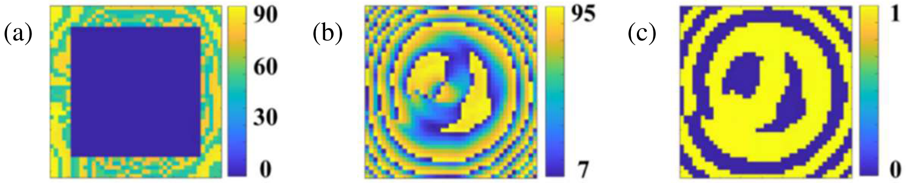

**FIGURE 11.** The geometry parameter distributions for the planar MTS: (a) for $\beta$, (b) for $l$, and (c) for the unit and mirror unit.

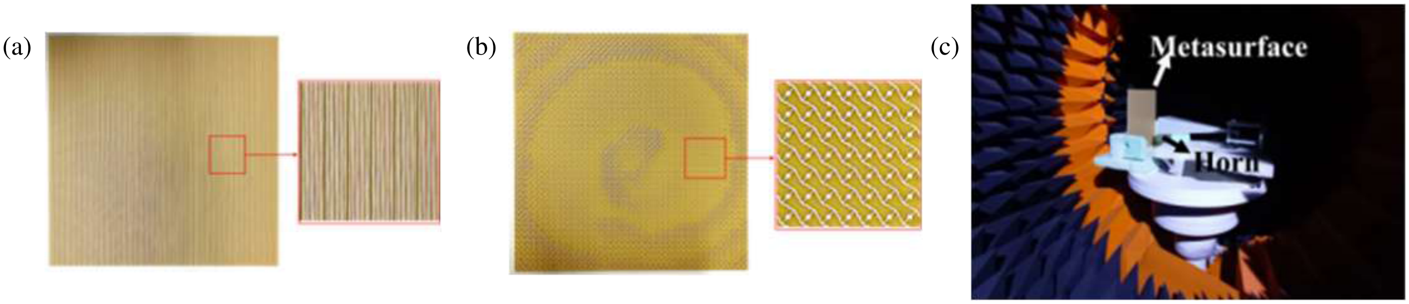

**FIGURE 12.** The prototype of the planar MTS: (a) the top (bottom) layer and their detailed drawing, (b) the top side of the dual middle metal layers and its detailed drawing, (c) the measurement environment.

## 4. SIMULATED AND MEASURED RESULTS

To confirm the PAM-PM combined design strategy for the conformal MTS with high SNR and FE, four transmission MTSs with the same size of 351 mm×351 mm ($14.04\lambda \times 14.04\lambda$, $\lambda$ wavelength) formed by $60 \times 60$ unit cells are researched and compared at 12 GHz: cylindrical conformal MTS-1 (PAM-PM), planar MTS-2 (PAM-PM), cylindrical conformal MTS-3 (PM), and planar MTS-4 (PM). The planar MTS with PAM-PM has been fabricated, and Fig. 12 is the prototype and measurement environment. Fig. 12(a) shows the top (or bottom) layer of the planar MTS and its detailed drawing, and Fig. 12(b) is the top side of the dual middle metal layers and their detailed drawing. Fig. 12(c) illustrates the testing environment in the

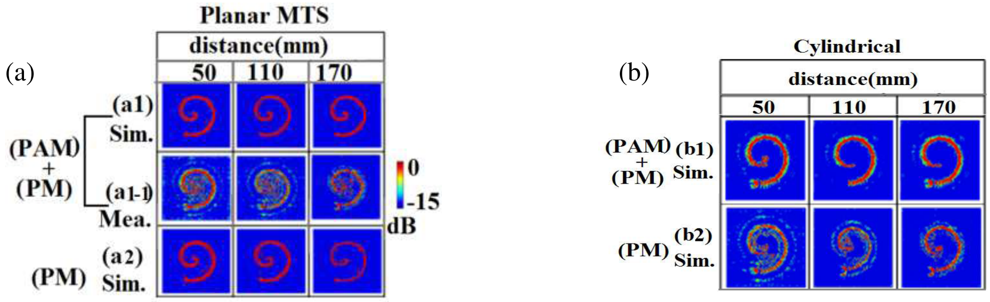

**FIGURE 13.** Simulation or measured $E$-fields in $xoy$ plane of the 3D spiral shaped near field at $z = 50$ mm, 110 mm, 170 mm: (a) for the planar MTS, (b) Simulated field for the cylindrical conformal MTS.

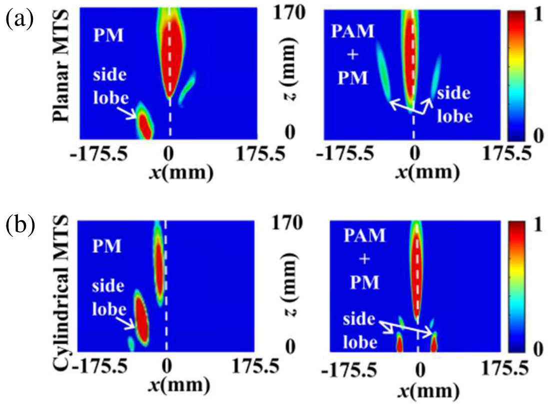

**FIGURE 14.** The simulated normalized $E$-field distributions in $xoz$ plane at 12 GHz: for planar MTSs with PM or PAM-PM (a), for cylindrical conformal MTSs with PM or PAM-PM (b).

anechoic chamber. A KEYSIGHT E5071C Vector Network Analyzer (VNA) was used to test the shaped $E$-field distribution. The distance between the MTS and the horn is 350 mm. The simulated or measured normalized $E$-field distributions in the cross section ($xoy$ plane at a distance $z = 50$ mm, 110 mm, and 170 mm) of the field of the 3D near field with spiral-shaped cross section are shown in Fig. 13. Figs. 13(a) and 13(b) are for planar and cylindrical conformal MTSs, respectively. Figs. 13(a1) and (a1-1) are the simulated and measured $E$-field distributions for the planar MTS with PAM-PM. There is some noise in the measured result because structural defects are introduced unintentionally during the fabrication due to the subwavelength size of the unit cells and the test environment. Fig. 13(a2) is the $E$-field for planar MTS with PM. Figs. 13(b1) and 13(b2) are the simulated $E$-field distributions for the cylindrical conformal MTSs with PAM-PM and PM, respectively. The SNR is defined as the ratio of the peak intensity of the image to the standard deviation of the background noise. There exists noise for the $E$-field distributions for cylindrical conformal MTSs; however, the cylindrical conformal MTS with PAM-PM greatly reduces the noise. The planar MTS with PAM-PM or PM has a clear simulated image and exhibits a better SNR than cylindrical conformal MTSs.

Figure 14 shows the simulated normalized $E$-field distributions in the $xoz$ plane at $y = 0$ at 12 GHz for MTSs with PM or PAM-PM. Figs. 14(a) and 14(b) are for planar MTSs and cylindrical conformal MTSs, respectively. For planar MTS, the simulated $E$-fields have low side lobe and high SNR for both the PM and PAM-PM MTSs. For cylindrical conformal MTSs, there exists some noise in the background for PM, and the PAM-PM greatly improves the SNR. The $E$-field distributions remain unchanged in the diffraction-free distance (within the $z$-axis range of 50–170 mm), and the $E$-field is very little between the MTS and focusing point, which is important in practical applications for safety. Both the cylindrical conformal and planar MTSs with PM or PAM-PM exhibit good SNR in the $xoz$ planar. However, there exist side lobes (marked in Fig. 14), due to the coupling among adjacent units.

The focusing efficiency ($\eta$) (FE) of the MTS is calculated by $\eta_{\text{focus}} = P_1/P$ [22], where $P_1$ is the shaped near-field power in $xoy$ plane $S$, and $P_0$ is the power from the horn. The size of the integral plane ($S$) is 175.5 mm×175.5 mm.

$$P_1 = \int_S \frac{1}{2}\text{Re}\left(\vec{E} \times \vec{H}^*\right) \cdot \vec{n} ds$$
$$\eta_{\text{focus}} = \frac{P_1}{P_0} \tag{6}$$

The maximum FE is achieved at $d = 110$ mm, and the FE decreases as the distance increases. For the cylindrical conformal MTSs, the FEs are 33.2% and 38.1% for PM and PAM-PM, respectively. For the planar MTSs, the FEs are 37.1% and 38.5% for PM and PAM-PM, respectively. The PAM-PM MTSs have higher FE than the PM MTSs.

A comparison between the proposed and recently published shaped near-field MTSs has been made in Table 1. (1) For 3D

**TABLE 1**. Comparison between the work with PAM in this paper and recently published shaped near-field MTSs.

| Ref. | Type | Fre. (GHz) | modulation | Focusing position control | $\eta_{\text{focus}}$ (%) | shaped near field |
|---|---|---|---|---|---|---|
| [11] | Huygens' MTS | 5.8 | PM | No | - | 3D Helical Beams |
| [12] | Planar MTS | 16∼30 | PM | No | 30.5 | (3D) 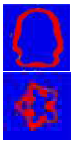 |
| [23] | holographic tensor impedance MTS (conformal) | 30 | Impedance | Yes | 42.1 | 2D rectangle  |
| This work | amplitude-phase control metasurface (conformal) | 12 | PAM | Yes | 38.1 | 3D Spiral-shaped 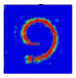 |

near-field comparison. Refs. [11, 12] and the proposed work are 3D near fields. Refs. [11, 12] are planar MTS with PM, and the proposed work is a conformal MTS with PAM-PM. The proposed field and [12] generate 3D-shaped near fields with arbitrary cross section (field structural complexity comparison); however, the proposed 3D-shaped near field has controlled spatial position from $Z = 50\,\text{mm}$ to 170 mm, and refs. [11, 12] do not have the function (field shaping accuracy comparison). In addition, the proposed 3D has the highest FE for the 3D-shaped field 38.1%; ref. [12] is 30.5%; and the FE of [11] is not provided (efficiency comparison). (2) For conformal MTS comparison. Ref. [23] is a conformal MTS and has the highest FE 42.1%. However, the shaped near field in [23] is a 2D rectangle (structural complexity comparison). The proposed work with PAM-PM simultaneously possesses the following performance: conformality, high FE, 3D-shaped near field with controlled spatial position, and high SNR. (3) Both the 3D near fields generated by the planar MTSs [12, 23] and the proposed conformal MTS with PAM-PM have clear 3D field images and validate the effectiveness of the proposed conformal MTS PAM-PM modulation technique in improving the SNR and efficiency. (4) For Operating Frequency. The conformal MTS works at a single frequency 12 GHz. Ref. [12] operates at 16–30 GHz, and [11, 23] work at 30 GHz. (5) The MTSs in [11, 12] are planar structures, and [23] and the proposed MTSs are conformal, so it is easier to fabricate planar MTS than curved MTS.

## 5. CONCLUSION

In this paper, a PAM-PM combined modulation technique is proposed for a conformal MTS. For conformal MTS, there exists an oblique incidence effect, and the following modulation strategy is used: (1) PAM for the units under an oblique incidence angle $\theta > 40^\circ$. (2) PM with constant amplitude for the units with $\theta < 40^\circ$. The phase and amplitude of the unit are obtained by the PC technique. A 3D-shaped propagation field with a spiral-shaped cross section (in $xoy$ plane) and linear propagation trajectory (in $z$ coordinate axis direction) is generated by four MTSs, respectively. Research indicates: (1) For planar MTS, the SNR is almost the same for PM and PAM-PM techniques. (2) For conformal MTS, PAM-PM has a higher SNR and FE than PM. The designed cylindrical conformal MTS with PAM+PM simultaneously possesses the following advantages: conformality, high FE (38.1%), high SNR (above 13 dB), 3D shaped near field, and controlled spatial position (from $z = 50\,\text{mm}$ to 170 mm).

## ACKNOWLEDGEMENT

This work was supported by the Guangdong Major Project of Basic and Applied Basic Research (2023B0303000008), the National Key Research and Development Program of China (2020YFB1807300), and the State Key Laboratory of Radio Frequency Heterogeneous Integration (Shenzhen University) No. 202306.

## REFERENCES

[1] Hajiahmadi, M. J., R. Faraji-Dana, and C. Caloz, "Metasurface-based time-reversal focusing for brain tumor microwave hyperthermia," *IEEE Transactions on Antennas and Propagation*, Vol. 70, No. 12, 12 237–12 246, 2022.

[2] Henriksson, T., N. Joachimowicz, C. Conessa, and J.-C. Bolomey, "Quantitative microwave imaging for breast cancer detection using a planar 2.45 GHz system," *IEEE Transactions on Instrumentation and Measurement*, Vol. 59, No. 10, 2691–2699, Oct. 2010.

[3] Zhong, S., "Progress in terahertz nondestructive testing: A review," *Frontiers of Mechanical Engineering*, Vol. 14, No. 3, 273–281, 2019.

[4] Zhang, Y., C. Wang, B. Huai, S. Wang, Y. Zhang, D. Wang, L. Rong, and Y. Zheng, "Continuous-wave THz imaging for biomedical samples," *Applied Sciences*, Vol. 11, No. 1, 71, 2021.

[5] Zhao, D. and M. Zhu, "Generating microwave spatial fields with arbitrary patterns," *IEEE Antennas and Wireless Propagation Letters*, Vol. 15, 1739–1742, 2016.

[6] Li, Y., N. Kou, and S. Yu, "Partially excited antenna array for near-field patterned focusing," *Progress In Electromagnetics Research Letters*, Vol. 105, 149–154, 2022.

[7] Huang, H.-F. and Z.-Y. Xiang, "Generating arbitrary shaped near-field with arbitrary polarization by combining tensor holographic impedance metasurface and phase conjugation techniques," *IEEE Antennas and Wireless Propagation Letters*, Vol. 23, No. 7, 1971–1975, 2024.

[8] Melamed, T., "Pulsed three-dimensional caustic beams over a generic curved trajectory in free space," in *2024 IEEE INC-USNC-URSI Radio Science Meeting (Joint with AP-S Symposium)*, 324–324, Florence, Italy, 2024.

[9] Guo, X., J. Zhong, B. Li, S. Qi, Y. Li, P. Li, D. Wen, S. Liu, B. Wei, and J. Zhao, "Full-color holographic display and encryption with full-polarization degree of freedom," *Advanced Materials*, Vol. 34, No. 3, 2103192, 2022.

[10] Zhang, S., W. Fan, K. J. Malloy, S. R. J. Brueck, N. C. Panoiu, and R. M. Osgood, "Near-infrared double negative metamaterials," *Optics Express*, Vol. 13, No. 13, 4922–4930, 2005.

[11] Su, D., H. Zhang, H. Xiao, W. Song, H. Xiong, D. Xiao, and X. Wang, "Construction of 3-D microwave helical beams using Huygens' metasurface," *IEEE Transactions on Antennas and Propagation*, Vol. 71, No. 11, 8907–8916, Nov. 2023.

[12] Huang, H.-F. and K.-C. Niu, "Phase gradient metasurface for arbitrary three-dimensional shaped near-field," *Optics Continuum*, Vol. 3, No. 10, 1846–1855, 2024.

[13] Williams, D. E., C. Dorn, S. Pellegrino, and A. Hajimiri, "Origami-inspired shape-changing phased array," in *2020 50th European Microwave Conference (EuMC)*, 344–347, Utrecht, Netherlands, 12-14 2021.

[14] Liang, H.-Y., H.-C. Yang, and J. Zhang, "A cylindrical conformal directional monopole antenna for borehole radar application," *IEEE Antennas and Wireless Propagation Letters*, Vol. 11, 1525–1528, 2012.

[15] Chávez-cerda, S., "A new approach to bessel beams," *Journal of Modern Optics*, Vol. 46, No. 6, 923–930, 1999.

[16] Zhong, Y. C. and Y. J. Cheng, "Ka-band wideband large depth-of-field beam generation through a phase shifting surface antenna," *IEEE Transactions on Antennas and Propagation*, Vol. 64, No. 12, 5038–5045, 2016.

[17] Lou, Q. and Z. N. Chen, "Sidelobe suppression of metalens antenna by amplitude and phase controllable metasurfaces," *IEEE Transactions on Antennas and Propagation*, Vol. 69, No. 10, 6977–6981, 2021.

[18] Guo, W.-L., G.-M. Wang, X.-Y. Luo, K. Chen, H.-P. Li, and Y. Feng, "Dual-phase hybrid metasurface for independent amplitude and phase control of circularly polarized wave," *IEEE Transactions on Antennas and Propagation*, Vol. 68, No. 11, 7705–7710, 2020.

[19] Abdelrahman, A. H., F. Yang, A. Z. Elsherbeni, and P. Nayeri, *Analysis and Design of Transmitarray Antennas*, Springer, 2017.

[20] Qin, P.-Y., L.-Z. Song, and Y. J. Guo, "Beam steering conformal transmitarray employing ultra-thin triple-layer slot elements," *IEEE Transactions on Antennas and Propagation*, Vol. 67, No. 8, 5390–5398, 2019.

[21] Wang, Q., X. Zhang, E. Plum, Q. Xu, M. Wei, Y. Xu, H. Zhang, Y. Liao, J. Gu, J. Han, and W. Zhang, "Polarization and frequency multiplexed terahertz meta-holography," *Advanced Optical Materials*, Vol. 5, No. 14, 1700277, 2017.

[22] Zhang, T. Y., S. Sun, Y. Gou, H. L. Wang, H. F. Ma, and T. J. Cui, "Frequency-multiplexed holographic-reflective coding metasurface for independent controls of surface wave and spatially propagating wave," *Advanced Optical Materials*, Vol. 11, No. 10, 2202832, 2023.

[23] Huang, H. and Z. Xiang, "Near-field shaping with arbitrary patterns and poarization by conformal tensor impedance modulated holographic metasurfaces," *Progress In Electromagnetics Research Letters*, Vol. 123, 1–6, 2025.